

Device simulation of liquid crystal polarization gratings

JIANGHAO XIONG,¹ RAN CHEN,^{1,2} AND SHIN-TSON WU^{1,*}

¹College of Optics and Photonics, University of Central Florida, Orlando, Florida 32816, USA

²School of Materials Science and Engineering, Shaanxi Normal University, Xi'an 710119, China

*swu@creol.ucf.edu

Abstract: Liquid crystal polarization gratings manifest several unique features, such as high diffraction efficiency, polarization selectivity, and fast switching time. However, few works address the chiral-doped liquid crystal alignment issue in such gratings. Here, we develop an improved relaxation method to analyze the liquid crystal director distribution in chiral-doped polarization gratings. Our simulation result agrees well with experimental data on a polarization volume grating. The criteria for forming planar or slanted polarization grating are discussed.

© 2019 Optical Society of America under the terms of the [OSA Open Access Publishing Agreement](#)

1. Introduction

Liquid crystal polarization grating (LCPG) is a critical optical element in near-eye displays because of its high diffraction efficiency and polarization selectivity [1–6]. Two types of LCPG have been developed: half-wave polarization grating (HWPG) [3–9] and polarization volume grating (PVG) [1,2,10–13]. HWPG utilizes the periodic change of Pancharatnam-Berry phase [13,14] resulting from the rotating optical axis along the x -axis, as Fig. 1(a) depicts. The simplest HWPG is composed of nematic liquid crystal (LC) that forms half-wave plate with spatially rotating optical axis. However, it usually has limited angular and spectral bandwidths. In order to improve its optical performance, multi-layer structure with chiral dopants is proposed [7–9]. The chiral dopant induces cholesteric liquid crystal (CLC) and offers a way to manipulate the twisting angle. However, the LC director distribution is presumed intuitively to be planar and multiple spin-coatings are adopted to overcome the critical thickness issue. The LC director deformation due to chiral dopants and weak anchoring strength of the pattern is not considered. Although some previous works address on the nematic LC alignment in LCPGs [16,17], to the best of our knowledge, no rigorous analysis dealing with the CLC case and weak anchoring condition has been reported. Hence, detailed theoretical analyses of alignment condition in terms of pattern period, anchoring strength, CLC pitch, and HWPG thickness is urgently needed.

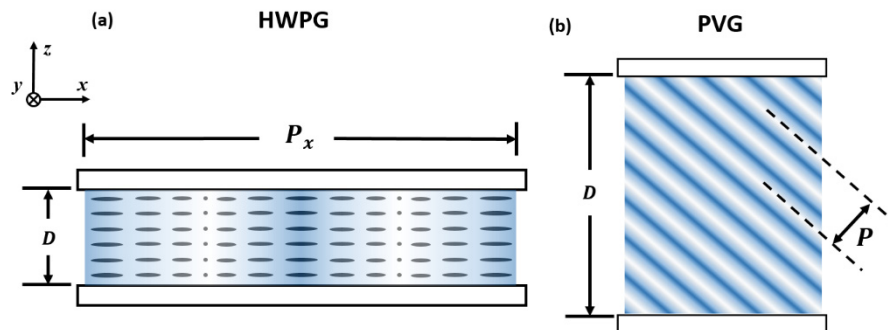


Fig. 1. Schematic plot of (a) HWPG and (b) PVG. The pitch corresponds to LC director rotating from 0 to 2π .

PVG, on the other hand, utilizes the periodic volumetric modulation of electric susceptibility tensor caused by the change of the LC director axis, as shown in Fig. 1(b). The grating thickness (D) is usually much larger than the grating period (P) in order to establish efficient Bragg diffraction. PVG can either be fabricated through multiple spin-coating process [1,2], one-time spin-coating [11], or cell formation [12]. In the past studies, the LC director distribution was often assumed planar because the bottom alignment is planar. Until recently, some experimental evidences suggest that the actual LC director configuration in a PVG may not be planar; instead, it possesses slanted structure [13]. Different LC configurations lead to different optical performance. Thus, to build an accurate simulation model for understanding the LC director distribution in a PVG and analyzing its electro-optic effect is in urgent need.

Although the optical performances of HWPG and PVG are different, their fabrication processes are rather similar: begin with a patterned alignment layer and then overcoat a LC layer with different thickness and chiral concentration. Therefore, the basic simulation model for both structures is the same. The equilibrium of the LC directors corresponds to the minimal free energy described by Frank-Oseen model [18]. Several numerical methods have been proposed to find the free energy minima, including directly solving Euler-Lagrange equations [15–20], Monte-Carlo method [21–24], and relaxation method [17,24,25]. Directly solving Euler-Lagrange equations provides detailed physical insights. It is suitable for systems with one spatial variable [17–20] or separable using a proper approximation [16]. However, in a LCPG with high chiral concentration, the director field is dependent on two highly coupled spatial variables, which makes analytically solving the Euler-Lagrange equations difficult. In Monte-Carlo method, the simulated annealing algorithm is usually applied to allow the acceptance of higher energy state in order to jump out of the local minima. If the annealing temperature decreases slowly and the number of iterations is sufficient, then finding global minima is feasible. However, the required number of iterations could be very large, making the simulation too time-consuming for studying different configurations of the system. Relaxation method adopts the principle of LC dynamics and uses the restoring force for the change of director in each iteration. However, when the concentration of chiral dopants is high, the relaxation method could be trapped in local minima and the final state is strongly dependent on the choice of initial state [24].

In this paper, we improve the relaxation method in two ways. First, we apply a weak balance condition technique to correct the algorithm that would otherwise give inaccurate and unstable results. Second, we accelerate the algorithm by seven times with momentum gradient descent method [26]. Using this improved relaxation method, we explore the LC director field in PVG with various scenarios and confirm our simulation results with experiment. Next, we apply our model to analyze the performance of HWPG. To maintain planar structure, for a large deflection angle multi-layer HWPG with chiral dopants, the maximum thickness of each layer should not exceed ~ 20 nm, while for a small deflection angle HWPG the maximum thickness of each layer is about 600 nm.

2. Simulation method

With an external electric field, the Frank-Oseen free energy density has following expression:

$$f_v = \frac{1}{2} K_1 (\nabla \cdot \hat{n})^2 + \frac{1}{2} K_2 (\hat{n} \cdot \nabla \times \hat{n} + \frac{2\pi}{P})^2 + \frac{1}{2} K_3 |\hat{n} \times \nabla \times \hat{n}|^2 - \frac{1}{2} \epsilon_0 \Delta \epsilon (\vec{E} \cdot \hat{n})^2, \quad (1)$$

where $\hat{n} = (\cos \theta \cos \phi, \cos \theta \sin \phi, \sin \theta) = (n_x, n_y, n_z)$ represents the LC director field, K_1 , K_2 , and K_3 are the corresponding splay, twist, and bend elastic constants, and P is the helical pitch of the CLC. It should be pointed out that here we use pitch to represent the LC director rotating from 0 to 2π , which is twice the optical pitch because the LC director repeats after rotating 180° . The total free energy is obtained by integrating the free energy density over the

volume: $F_v = \int f_v dV$. The minimization of total free energy is a constrained variational problem, which needs to include a Lagrange multiplier $\lambda(x, y, z)$. The corresponding Euler-Lagrange equations are expressed as

$$H_i \equiv -\frac{\partial f_v}{\partial n_i} + \sum_j \partial_j \left(\frac{\partial f_v}{\partial (\partial_j n_i)} \right) = -\lambda n_i, i = 1, 2, 3, \quad (2)$$

where $\partial_j \equiv \partial / \partial x_j$ and $j = 1, 2$, and 3 . The left-hand side of Eq. (2) is often noted as molecular field. The equilibrium condition is achieved when the molecular field is parallel to the LC director. The relaxation method updates the LC director towards the molecular field in each iteration

$$\Delta n_i = \omega h_i, \quad (3)$$

$$h_i = H_i - (\vec{H} \cdot \hat{n}) n_i, \quad (4)$$

where h_i is the molecular field projected perpendicular to the director, ω is the relaxation constant that can be adjusted to get faster convergence speed. The relaxation method is in its nature a first-order gradient descent method because the molecular field comes from the first-order variation of the free energy. Momentum gradient descent (MGD) algorithm [26] is used to accelerate the update

$$\Delta \hat{n}_t = \omega \vec{h}_t + \beta \Delta \hat{n}_{t-1}, \quad (5)$$

where the subscript t means current iteration and $(t-1)$ is the last iteration, and β is a value typically set between 0.8 and 0.9. It should be noted that $\Delta \hat{n}_{t-1}$ contains the values of all previous updates, with exponentially decreasing weight. Hence, MGD accumulates momentum when going downhill, which accelerates the update, but it slows down the update when the system hits the plateau. Using MGD, our simulation speed is improved by $\sim 7x$ on average.

The handling of boundaries is extremely important in the simulation. The LCPG is uniform in the y direction, so only x and z directions are considered. The length of the simulation region in x direction is the same as the x period, with director rotating from 0 to 2π . So periodic condition is applied on x boundaries. Note that in practical fabrications of HWPG and PVG, either reactive mesogen (RM) is spin-coated onto the patterned photo-alignment film, or the LC material is infiltrated into a cell with one patterned alignment surface. In both cases, only one surface is patterned, while the other side is in contact with air or glass, to form homeotropic anchoring (or planar anchoring if surfactant is added). The bottom surface is usually coated with photo-alignment material patterned by interferometer exposure. The anchoring strength of photo-alignment surface can range from 10^{-6} J/m² to 10^{-4} J/m² [27], depending on the material and exposure dosage. Therefore, the general form of weak anchoring is adopted for both surfaces. The top interfacial energy density is

$$f_{s,t} = -\frac{1}{2} W_t (\hat{n} \cdot \hat{z})^2 = -\frac{1}{2} W_t \sin^2 \theta, \quad (6)$$

where W_t is the anchoring strength; $W_t < 0$ means planar anchoring while $W_t > 0$ means homeotropic anchoring. The bottom surface energy density is

$$f_{s,b} = -\frac{1}{2} W_b (\hat{n} \cdot \hat{e})^2 = -\frac{1}{2} W_b \cos^2 \theta \cos^2 \left(\phi - \frac{2\pi}{P_x} x \right), \quad (7)$$

where P_x is the pattern period (Fig. 1(a)). The general form of the torque balance equation for a weak anchoring boundary is [20]

$$\frac{\partial f_v}{\partial(\partial_z \theta)} + \frac{\partial f_s}{\partial \theta} = 0, \quad (8)$$

$$\frac{\partial f_v}{\partial(\partial_z \phi)} + \frac{\partial f_s}{\partial \phi} = 0, \quad (9)$$

where f_s is the surface energy density.

The physical meaning of the first terms of Eqs. (8) and (9) is the change of bulk elastic free energy due to the change of z derivatives of θ and ϕ , while the second terms mean the change of surface interfacial energy.

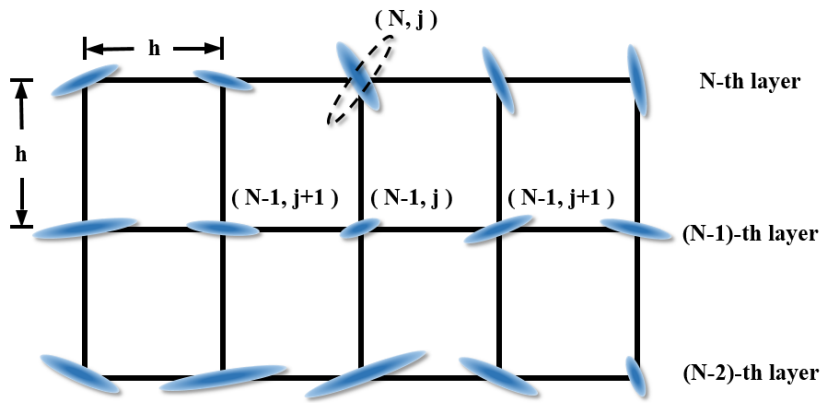


Fig. 2. Schematic drawing of simulation grid. The N^{th} layer is the top layer of the simulation region and h is the grid size.

In the simulation, finite difference method is used for discretization of the simulation region, as shown in Fig. 2. The top N -th layer only has surface energy while the layers beneath have bulk free energy. The change of the (N, j) grid point in the top layer only influences the bulk free energy of the $(N-1, j)$ point through the change of the z derivatives of $(N-1, j)$ point, while the calculation of x derivatives of the $(N-1)$ -th layer is irrelevant of the N -th layer. Therefore, the numerical calculation of $\partial f_v / \partial(\partial_z \theta)$ and $\partial f_v / \partial(\partial_z \phi)$ of $(N-1, j)$ point only uses the N -th layer through the calculation of $\partial_z \theta$ and $\partial_z \phi$. Considering that the free energy is the quadratic function of first derivatives of θ and ϕ , the $\partial f_v / \partial(\partial_z \theta)$ and $\partial f_v / \partial(\partial_z \phi)$ terms only contain the linear forms of θ_N and ϕ_N . The second terms in Eqs. (8) and (9), $\partial f_s / \partial \theta$ and $\partial f_s / \partial \phi$, also use θ_N and ϕ_N for calculation. As a result, the general forms of Eqs. (8) and (9) are transcendental. Therefore, Newton's iteration is adopted to solve the equations.

Without losing generality, the bottom (1st) layer is used for illustration. Here $\tilde{\theta}, \tilde{\phi}$ and \tilde{n}_i are used to denote the values of second layer. Then Eqs. (8) and (9) can be expanded as:

$$f_1(\theta, \phi) = -\frac{\tilde{F}_1}{h} \theta + \frac{\tilde{F}_1}{h} \tilde{\theta} + \tilde{G}_1 + \frac{1}{2} W_b \sin 2\theta \cos^2 \Delta\phi = 0, \quad (10)$$

$$f_2(\theta, \phi) = -\frac{\tilde{F}_2}{h} \theta + \frac{\tilde{F}_2}{h} \tilde{\theta} + \tilde{G}_2 + \frac{1}{2} W_b \cos^2 \theta \sin 2\Delta\phi = 0, \quad (11)$$

$$\Delta\phi = \phi - \frac{2\pi}{P_x} x, \quad (12)$$

$$\tilde{F}_1 = (K_1 \cos^2 \tilde{\theta} + K_3 \sin^2 \tilde{\theta}), \quad (13)$$

$$\tilde{F}_2 = (K_2 \cos^2 \tilde{\theta} + K_3 \sin^2 \tilde{\theta}) \cos^2 \tilde{\theta}, \quad (14)$$

$$\tilde{G}_1 = K_1 \partial_x \tilde{n}_x \cos \tilde{\theta} + K_3 \partial_x \tilde{n}_z \sin \tilde{\theta} \cos \tilde{\phi}, \quad (15)$$

$$\begin{aligned} \tilde{G}_2 = & -K_2 (q + \tilde{n}_z \partial_x \tilde{n}_y - \tilde{n}_y \partial_x \tilde{n}_z) \cos^2 \tilde{\theta} + \\ & K_3 (\cos^2 \tilde{\theta} \sin \tilde{\theta} \partial_x \tilde{n}_y + \sin^2 \tilde{\theta} \cos \tilde{\theta} \partial_x \tilde{n}_z \sin \tilde{\phi}). \end{aligned} \quad (16)$$

All symbols with \sim are calculated using the second layer and therefore can be treated as constants. After some algebra, we derive the Jacobian for (f_1, f_2) as:

$$J = \begin{pmatrix} \frac{\partial f_1}{\partial \theta} & \frac{\partial f_1}{\partial \phi} \\ \frac{\partial f_2}{\partial \theta} & \frac{\partial f_2}{\partial \phi} \end{pmatrix} = \begin{pmatrix} -\frac{\tilde{F}_1}{h} + W_b \cos 2\theta \cos^2 \Delta\phi & -\frac{1}{2} W_b \sin 2\theta \sin 2\Delta\phi \\ -\frac{1}{2} W_b \sin 2\theta \sin 2\Delta\phi & -\frac{\tilde{F}_2}{h} + W_b \cos^2 \theta \cos 2\Delta\phi \end{pmatrix}. \quad (17)$$

In each Newton's iteration, (θ, ϕ) is updated according to

$$\begin{pmatrix} \theta_{t+1} \\ \phi_{t+1} \end{pmatrix} = \begin{pmatrix} \theta_t \\ \phi_t \end{pmatrix} - J^{-1} \begin{pmatrix} f_1(\theta_t, \phi_t) \\ f_2(\theta_t, \phi_t) \end{pmatrix}. \quad (18)$$

For each calculation of the bottom director field, we start the Newton's iteration using result from the last calculation. The ending condition of the iterations is set as when f_1 and f_2 are less than $10^{-4} \mu\text{N/m}$. Typically, it takes only 3 iterations to reach the ending condition, so the computational burden of the bottom field is negligible.

Here the solutions are noted as θ_N^s and ϕ_N^s . It is straightforward to use θ_N^s and ϕ_N^s for the top layer for each iteration. It is found, however, that the system tends to form local defects and does not reach the lowest energy state if we do so. For illustration, a PVG with mono-elastic-constant of $10 pN$ is simulated. The grating period is 800 nm, the thickness is 2 μm , and CLC pitch is 400 nm. The anchoring strength is $W_t = 3 \mu\text{N/m}$ and $W_b = 100 \mu\text{N/m}$. The result of the director field is plotted in Fig. 3(a), and the free energy density is in Fig. 3(b). It can be seen that many high-energy defects are formed, which contradicts with the experimental observation on the formation of a good performance PVG. Furthermore, the final state is strongly dependent on the initial state, which makes the simulation results unpredictable if the initial state is random. To overcome these issues, we add a modification to the updating method of the top and bottom layers, denoted as weak balance condition.

This method takes into account that the bulk distribution is iteratively evolving toward the equilibrium state instead of getting to it at once. It is therefore appropriate to keep surface and bulk updating at a relatively similar pace. For each update, instead of getting to the balance at once, we loosen the condition as

$$\theta_N = \alpha \theta_N^s + (1 - \alpha) \theta_{N-1}, \quad \phi_N = \alpha \phi_N^s + (1 - \alpha) \phi_{N-1}, \quad (19)$$

where α is a value to be adjusted in the iteration, the closer it is to 1, the better the balance is. In the simulation, we let α start from 0.7 to 0.8 and gradually increase it to 1. Using this technique, the local defects are able to rise to the top or bottom and then vanish, leading the system to the lowest energy state. As shown in Figs. 3(a) and 3(b), the final state is aligned

well without defects and the volume energy is close to zero, except for the region near the top surface where the weak homeotropic anchoring slightly deforms the CLC structure.

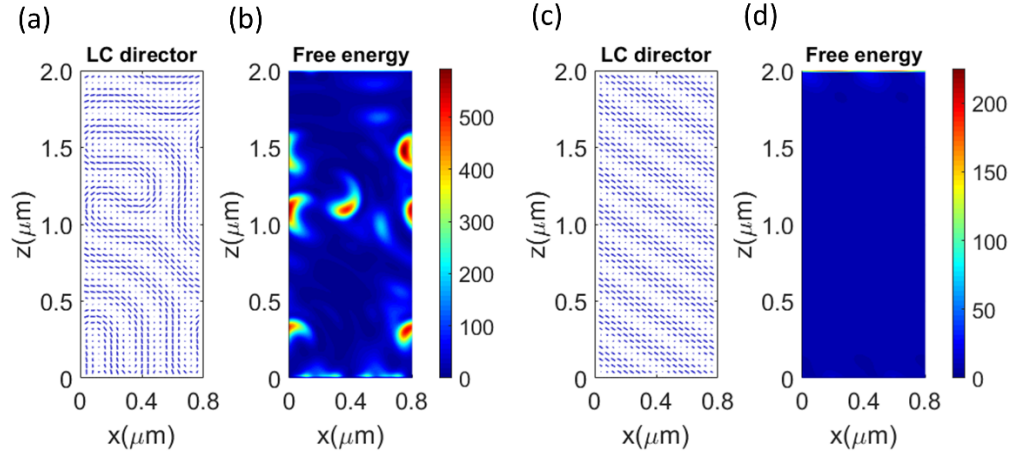


Fig. 3. Comparison of simulation results with and without weak balance condition (WBC). Simulated (a) director field and (b) free energy density without WBC. Simulated (c) director field and (d) free energy density with WBC. The unit of the scale bar is J/m^3 .

3. Results and discussion

3.1 PVG cell with an electric field

To validate our simulation model with experiment, we fabricated a PVG cell and measured its optical performance. First, we prepared a clean ITO (indium tin oxide) glass substrate treated with UV ozone (10 min.) and spin-coated on top a layer of photo-alignment material (Brilliant yellow 0.4% wt, 3000 rpm for 30s). Then we exposed the substrate with the interference pattern formed by a 488-nm laser for 8 minutes. The detailed setup of the exposure system has been described in [1]. The period of the alignment pattern P_x is 850 nm. Then another cleaned ITO glass was placed on top to form a cell with 2- μm gap. Then we infiltrated the LC into the cell, followed by heating the cell to clear point (120°C) and gradually cooling it down to the room temperature. The LC material used is MLC-2048 with 1.56wt.% chiral dopants S-5011 ($\text{HTP} = 107 \mu\text{m}^{-1}$). The pitch of the CLC is calculated to be $P_{clc} = 599 \text{ nm}$. The elastic constants of MLC-2048 were measured as $K_1 = 15.7 \text{ pN}$, $K_2 = 12.6 \text{ pN}$, and $K_3 = 36.4 \text{ pN}$. To see the voltage-dependent optical behavior, we applied an ac voltage of 8 kHz with different amplitude. The dielectric anisotropy of MLC-2048 at 8 kHz is $\Delta\epsilon = 1.0$. During simulation, the anchoring strength is set as $W_t = 3 \mu\text{N/m}$ and $W_b = 100 \mu\text{N/m}$. At $V = 0$, we start from a random initial state and let it evolve to imitate the cooling-down process. In the voltage-on state, we set the initial state at $V = 0$. After acquiring the director field, we use finite element analysis to simulate the transmission spectra. To improve precision, we also measured the wavelength-dependent refractive indices of MLC-2048, and fitted the experimental data with extended Cauchy equation [28]

$$n_{e,o} = A_{e,o} + \frac{B_{e,o}}{\lambda^2} + \frac{C_{e,o}}{\lambda^4}. \quad (20)$$

The fitting parameters for n_e are $A_e = 1.6950$, $B_e = -0.0015 \mu\text{m}^2$, and $C_e = 0.0035 \mu\text{m}^4$, while the fitting parameters for n_o are $A_o = 1.5200$, $B_o = -0.0212 \mu\text{m}^2$, and $C_o = 0.0044 \mu\text{m}^4$.

The measured transmission spectra and simulated spectra are plotted in Figs. 4(a), 4(c), and 4(e), while the simulated director fields are plotted in Figs. 4(b), 4(d), and 4(f),

respectively. Considering such a complex system, the overall agreement between experiment and simulation is reasonably good.

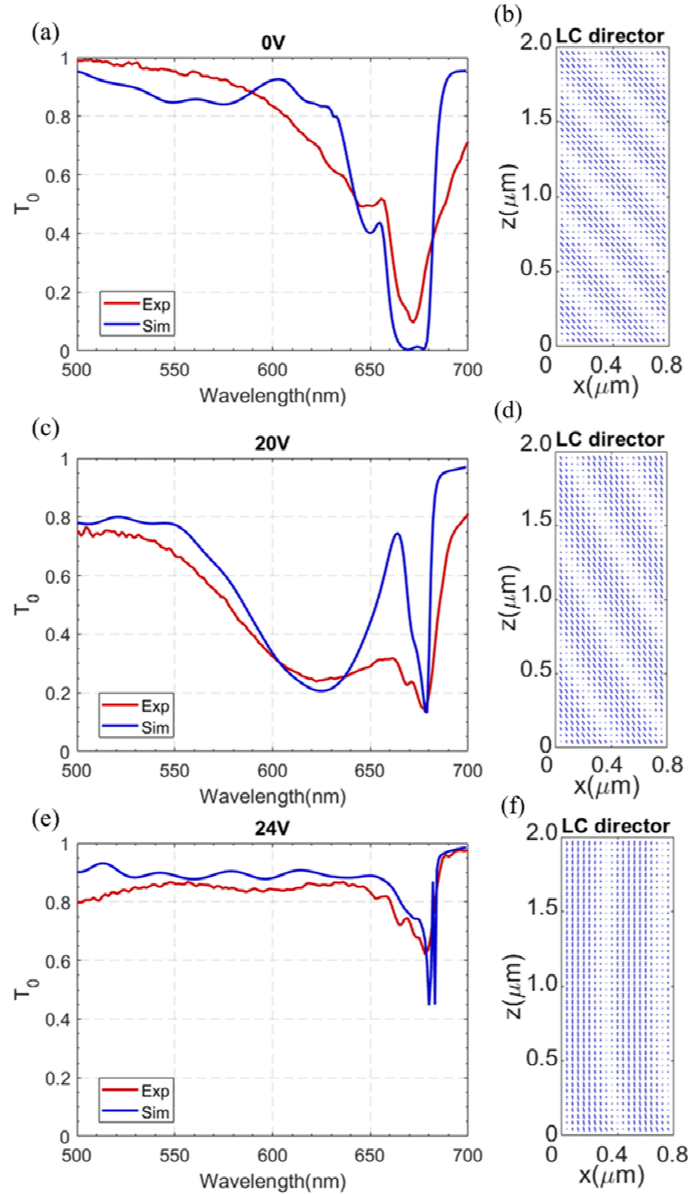


Fig. 4. Experimental and simulation results of zeroth order transmission spectrum of the PVG cell under different voltages. (a) Transmission spectrum and (b) simulated director field at $V = 0$. (c) Transmission spectrum and (d) simulated director field at $V = 20V_{\text{rms}}$. (e) Transmission spectrum and (f) simulated director field at $V = 24V_{\text{rms}}$.

At $V = 0$, the director field (Fig. 4(b)) is like a slanted CLC to ensure the lowest volume free energy. From Fig. 4(b), we find the periodicity of the simulated director in z -direction is $P_z = 847$ nm. Once P_z is obtained, we can calculate the total Bragg grating period P_B using following relation:

$$\frac{1}{P_x^2} + \frac{1}{P_z^2} = \frac{1}{P_B^2}. \quad (21)$$

From Eq. (21), we find $P_B = 600$ nm, which is nearly the same as P_{clc} (≈ 599 nm). This means in the completely relaxed state, the CLC pitch is equal to the Bragg pitch. Recently, Lee et al. [13] compared the optical performances of planar and slanted PVG configurations. They found that if the slant angle is $\approx 25^\circ$, then the agreement between experiment and simulation is very good. However, no detailed explanation was given. In our present analysis, the slant angle can be calculated through $\phi = \sin^{-1}(P_B / P_x) = \sin^{-1}(P_{clc} / P_x)$ and the result is 25.9° , which agrees with the reported experimental result well. *This data provides an important validation to our model.*

From Fig. 4(c), at $V = 20V_{rms}$, besides the peak located at 670 nm, another peak located at around 625 nm appears. This is because $P_x \approx P_z$ at $V = 0$, which means the grating lies at the boundary of transmissive and reflective ones. As the voltage increases, the director field is deformed, making P_z larger than P_x , so that the grating turns into transmission type [Fig. 4(d)]. The peak located at ~ 625 nm is the corresponding transmission peak.

As the voltage increases to $24 V_{rms}$, the transmission peak in the spectrum vanishes, leaving only one small peak at ~ 670 nm [Fig. 4(e)]. This is because the whole structure is deformed to be like a uniform lying helix (ULH) [19,29], as Fig. 4(f) depicts. Under such a circumstance, the center of the transmission peak blue shifts to zero and the peak at ~ 670 nm corresponds to the period of ULH, which is the same as P_x .

3.2 Alignment of thin LCPGs

To fabricate a HWPG with chiral dopants, multiple spin-coatings are adopted [7–9]. The purpose is to obtain thin layers of planar structure to control the twist angle of each layer and therefore manipulate the optical performance. Because in practical fabrication the formation of first passivation layer of RM can be adopted to improve the anchoring [9,30]. Considering the similarity of the molecular structure to the contacting layers, the anchoring strength is set as $W_b = 10^{-3}$ N/m, which falls into the strong anchoring category. For convenience, we define three unified dimensionless parameters

$$d = D / P_x, \quad (22)$$

$$p = P / P_x, \quad (23)$$

$$w_t = -W_t P_x / \bar{K}, \quad (24)$$

where \bar{K} is the average of the three elastic constants. With these parameters, the obtained simulation results can be extended to cases with different scales. The minus sign in (23) is because in the following discussion we will consider planar anchoring, which can be achieved by surfactant and adjusted by varying the concentration. To quantify the director deviation from the planar structure we also define the following parameter

$$\sigma = \sqrt{\langle (\hat{n} - \hat{n}_p)^2 \rangle}, \quad (25)$$

where \hat{n}_p is the planar director field defined as

$$\hat{n}_p = \left(\cos\left(\frac{2\pi}{P_x}x + \frac{2\pi}{P}z\right), \sin\left(\frac{2\pi}{P_x}x + \frac{2\pi}{P}z\right), 0 \right). \quad (26)$$

We study two cases with $p = \infty$ for nematic LC and $p = 0.5$ for CLC. In each case, we vary the thickness and top anchoring strength to see the change of deviation. Figure 5 depicts the

simulated results. For the cases without chiral dopant, as w_t increases the deformation is suppressed significantly. From Eq. (13), in order to increase w_t , we can either increase the surfactant concentration to increase anchoring strength, or increase the periodicity in x direction. It should be noted that in the limit of $w_t \rightarrow \infty$, the system degenerates into the case with two sides of strong anchoring. The director will still deform when $d > 0.5$ [17]. Figure 5 offers a good guidance to optimize the parameters when fabricating a HWPG. For example, with $W_t = -10^{-5}$ N/m, $\bar{K} = 10$ pN, and thickness is $1.5 \mu\text{m}$ to meet the half-wave condition, we can determine the minimum periodicity is $P_x = 10 \mu\text{m}$ so that $w_t = 10$ and $d = 0.15$ to allow the deviation $\sigma = 0.1$.

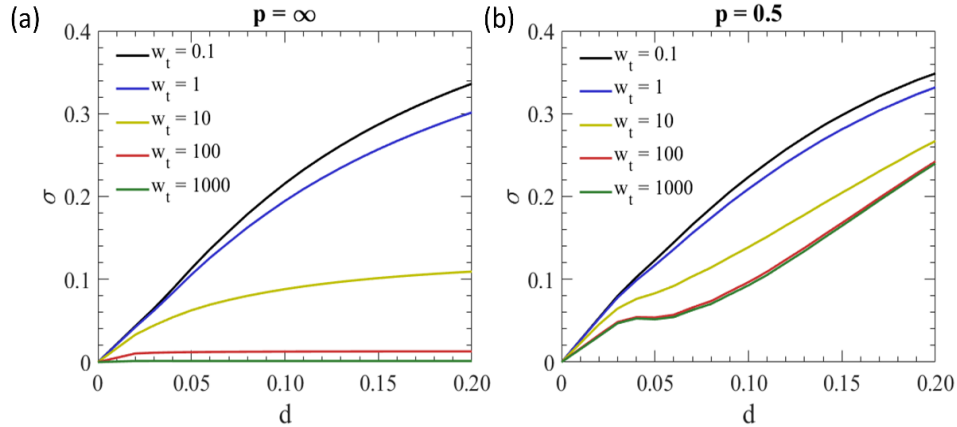


Fig. 5. LC director deformation with varying unified depth and top anchoring strength. (a) nematic LC without chiral dopant, and (b) CLC with $p = 0.5$.

For the CLC case (Fig. 5(b)), as w_t increases the deformation at small d values is suppressed to some degree and then saturates. The deformation at a relatively large d value is not effectively suppressed no matter how large w_t is. This means no matter how strong the anchoring at the top surface is, the LC directors will still quickly deform from the bottom planar structure to the slanted CLC shape. For the fabrication of multi-layer LCPGs, the requirement of deformation should be stricter because the deformation directly influences the alignment of next layer. If we allow the maximum deviation to be $\sigma = 0.05$, then, for example, in a system with $W_t = -10^{-4}$ N/m, $\bar{K} = 10$ pN, and $P_x = 1 \mu\text{m}$, we need to keep $d < 0.02P_x$, which is 20 nm. If $P_x = 10 \mu\text{m}$, then the condition is relaxed to $d < 0.06P_x$, which is 600 nm. In [31], the polarization grating with high chiral concentration is fabricated to achieve high deflection angle. The thickness of each layer in the multiple spin-coating is reported to be 55 nm in order to form a good pattern. This is in the same order of our analyzed result. The disparity of the exact values may come from the different choice of error tolerance of σ . Therefore, our analysis on the alignment condition is also validated.

4. Conclusion

A simulation model for the LC director field in chiral LCPGs is developed. The model is confirmed by explaining slanted angle of PVG in the previous work and comparing the experimental results with numerical prediction in a PVG cell with applied voltage. Then we discussed the alignment condition in the fabrication of LCPGs and offered a guidance of parameter selection.

Funding

Air Force Office of Scientific Research (FA9550-14-1-0279).

Acknowledgments

We are indebted to Kun Yin for help in device fabrication, and Guanjun Tan and Tao Zhan for useful technical discussions.

References

1. Y. H. Lee, K. Yin, and S. T. Wu, "Reflective polarization volume gratings for high efficiency waveguide-coupling augmented reality displays," *Opt. Express* **25**(22), 27008–27014 (2017).
2. Y. Weng, Y. Zhang, J. Cui, A. Liu, Z. Shen, X. Li, and B. Wang, "Liquid-crystal-based polarization volume grating applied for full-color waveguide displays," *Opt. Lett.* **43**(23), 5773–5776 (2018).
3. Y. H. Lee, G. Tan, T. Zhan, Y. Weng, G. Liu, F. Gou, F. Peng, N. V. Tabiryan, S. Gauza, and S. T. Wu, "Recent progress in Pancharatnam–Berry phase optical elements and the applications for virtual/augmented realities," *Opt. Data Process. Storage* **3**(1), 79–88 (2017).
4. Y. H. Lee, T. Zhan, and S. T. Wu, "Enhancing the resolution of a near-eye display with a Pancharatnam–Berry phase deflector," *Opt. Lett.* **42**(22), 4732–4735 (2017).
5. G. Tan, Y. H. Lee, T. Zhan, J. Yang, S. Liu, D. Zhao, and S. T. Wu, "Foveated imaging for near-eye displays," *Opt. Express* **26**(19), 25076–25085 (2018).
6. T. Zhan, Y. H. Lee, J. Xiong, G. Tan, K. Yin, J. Yang, S. Liu, and S. T. Wu, "High-efficiency switchable optical elements for advanced head-up displays," *J. Soc. Inf. Disp.* **27**(4), 223–231 (2019).
7. K. Gao, C. McGinty, H. Payson, S. Berry, J. Vornehm, V. Finnemeyer, B. Roberts, and P. Bos, "High-efficiency large-angle Pancharatnam phase deflector based on dual-twist design," *Opt. Express* **25**(6), 6283–6293 (2017).
8. C. Oh and M. J. Escuti, "Achromatic diffraction from polarization gratings with high efficiency," *Opt. Lett.* **33**(20), 2287–2289 (2008).
9. X. Xiang, J. Kim, and M. J. Escuti, "Bragg polarization gratings for wide angular bandwidth and high efficiency at steep deflection angles," *Sci. Rep.* **8**(1), 7202 (2018).
10. Y. Weng, D. Xu, Y. Zhang, X. Li, and S. T. Wu, "Polarization volume grating with high efficiency and large diffraction angle," *Opt. Express* **24**(16), 17746–17759 (2016).
11. J. Kobashi, Y. Mohri, H. Yoshida, and M. Ozaki, "Circularly-polarized, large-angle reflective deflectors based on periodically patterned cholesteric liquid crystals," *Opt. Data Process. Storage* **3**(1), 61–66 (2017).
12. R. Chen, Y. H. Lee, T. Zhan, K. Yin, Z. An, and S. T. Wu, "Multistimuli-responsive self-organized liquid crystal Bragg gratings," *Adv. Opt. Mater.* **7**(9), 1900101 (2019).
13. Y. H. Lee, Z. He, and S. T. Wu, "Optical properties of reflective liquid crystal polarization volume gratings," *J. Opt. Soc. Am. B* **36**(5), D9–D12 (2019).
14. S. Pancharatnam, "Generalized theory of interference and its applications," *Proc. Ind. Acad. Sci. A* **44**(6), 398–417 (1956).
15. M. V. Berry, "Quantal phase factors accompanying adiabatic changes," *Proc. R. Soc. Lond. A Math. Phys. Sci.*, **392**(1802), 45–57 (1984).
16. R. K. Komanduri and M. J. Escuti, "Elastic continuum analysis of the liquid crystal polarization grating," *Phys. Rev. E Stat. Nonlin. Soft Matter Phys.* **76**(2 Pt 1), 021701 (2007).
17. H. Sarkissian, B. Park, N. Tabirian, and B. Zeldovich, "Periodically aligned liquid crystal: potential application for projection displays," *Mol. Cryst. Liq. Cryst. (Phila. Pa.)* **451**(1), 1–19 (2006).
18. P. G. de Gennes, *The Physics of Liquid Crystals* (Oxford University, 1974).
19. G. Tan, Y. H. Lee, F. Gou, M. Hu, Y. F. Lan, C. Y. Tsai, and S. T. Wu, "Macroscopic model for analyzing the electro-optics of uniform lying helix cholesteric liquid crystals," *J. Appl. Phys.* **121**(17), 173102 (2017).
20. A. Sugimura, G. R. Luckhurst, and O. Y. Zhong-can, "Director deformation of a twisted chiral nematic liquid crystal cell with weak anchoring boundaries," *Phys. Rev. E Stat. Phys. Plasmas Fluids Relat. Interdiscip. Topics* **52**(1), 681–689 (1995).
21. I. Heynderickx, H. De Raedt, De Raedt H, "Calculation of the director configuration of nematic liquid crystals by the simulated-anneal method," *Phys. Rev. A Gen. Phys.* **37**(5), 1725–1730 (1988).
22. T. Gruhn and S. Hess, "Monte Carlo simulation of the director field of a nematic liquid crystal with three elastic coefficients," *Z. Naturforsch. A* **51**(1–2), 1–9 (1996).
23. R. W. Ruhwandl and E. M. Terentjev, "Monte Carlo simulation of topological defects in the nematic liquid crystal matrix around a spherical colloid particle," *Phys. Rev. E Stat. Phys. Plasmas Fluids Relat. Interdiscip. Topics* **56**(5), 5561–5565 (1997).
24. J. C. Armas-Pérez, J. P. Hernández-Ortiz, and J. J. de Pablo, "Liquid crystal free energy relaxation by a theoretically informed Monte Carlo method using a finite element quadrature approach," *J. Chem. Phys.* **143**(24), 243157 (2015).
25. H. Mori, E. C. Gartland, Jr., J. R. Kelly, and P. J. Bos, "Multidimensional director modeling using the Q tensor representation in a liquid crystal cell and its application to the π cell with patterned electrodes," *Jpn. J. Appl. Phys.* **38**(1), 135–146 (1999).
26. N. Qian, "On the momentum term in gradient descent learning algorithms," *Neural Netw.* **12**(1), 145–151 (1999).
27. V. P. Vorflusev, H. S. Kitzerow, and V. G. Chigrinov, "Azimuthal anchoring energy in photoinduced anisotropic films," *Jpn. J. Appl. Phys.* **34**(2), L1137–L1140 (1995).

28. J. Li and S. T. Wu, "Extended Cauchy equations for the refractive indices of liquid crystals," *J. Appl. Phys.* **95**(3), 896–901 (2004).
29. P. E. Cladis and M. Kleman, "The cholesteric domain texture," *Mol. Cryst. Liq. Cryst. (Phila. Pa.)* **16**(1–2), 1–20 (1972).
30. M. C. Tseng, O. Yaroshchuk, T. Bidna, A. K. Srivastava, V. Chigrinov, and H. S. Kwok, "Strengthening of liquid crystal photoalignment on azo dye films: passivation by reactive mesogens," *RSC Advances* **6**(53), 48181–48188 (2016).
31. X. Xiang, J. Kim, R. Komanduri, and M. J. Escuti, "Nanoscale liquid crystal polymer Bragg polarization gratings," *Opt. Express* **25**(16), 19298–19308 (2017).